

Thermal expansion and phase transformation in the rare earth di-titanate ($R_2\text{Ti}_2\text{O}_7$) system

Benjamin S. Hulbert, Scott J. McCormack, Kuo-Pin Tseng and Waltraud M. Kriven*

Materials Science and Engineering, University of Illinois at Urbana-Champaign, 1304 W Green St, Urbana, Illinois 61801, USA. *Correspondence e-mail: kriven@illinois.edu

Received 30 January 2021

Accepted 27 April 2021

Edited by O. V. Yakubovich, Moscow State University, Russian Federation

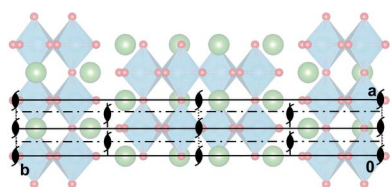
Keywords: rare earth di-titanate; X-ray diffraction; neutron diffraction; thermal expansion; phase transition; $\text{La}_2\text{Ti}_2\text{O}_7$; high-temperature.**CCDC references:** 2080398–2080430**Supporting information:** this article has supporting information at journals.iucr.org/b

Characterization of the thermal expansion in the rare earth di-titanates is important for their use in high-temperature structural and dielectric applications. Powder samples of the rare earth di-titanates $R_2\text{Ti}_2\text{O}_7$ (or $R_2\text{O}_3 \cdot 2\text{TiO}_2$), where $R = \text{La, Pr, Nd, Sm, Gd, Dy, Er, Yb, Y}$, which crystallize in either the monoclinic or cubic phases, were synthesized for the first time by the solution-based steric entrapment method. The three-dimensional thermal expansions of these polycrystalline powder samples were measured by *in situ* synchrotron powder diffraction from 25°C to 1600°C in air, nearly 600°C higher than other *in situ* thermal expansion studies. The high temperatures in synchrotron experiments were achieved with a quadrupole lamp furnace. Neutron powder diffraction measured the monoclinic phases from 25°C to 1150°C. The $\text{La}_2\text{Ti}_2\text{O}_7$ member of the rare earth di-titanates undergoes a monoclinic to orthorhombic displacive transition on heating, as shown by synchrotron diffraction in air at 885°C (864°C–904°C) and neutron diffraction at 874°C (841°C–894°C).

1. Introduction

The rare earth di-titanates, $R_2\text{Ti}_2\text{O}_7$ ($R = \text{rare earth element}$) or $R_2\text{O}_3 \cdot 2\text{TiO}_2$, form two types of structures at 25°C and 1 atm, some in a monoclinic, layered, perovskite-like structure and others in a cubic pyrochlore structure. Chemical compounds with the formula $A_2B_2O_7$ form the equilibrium structures described previously (Roth, 1956), where it was shown that the cation radius ratio between the larger cation radius, r_A , and the smaller cation radius, r_B , could be used to classify and predict crystal symmetry. For the rare earth di-titanate compounds (where $r_A = \text{rare earth ionic radius}$, $r_B = \text{titanium ionic radius}$) at 25°C and 1 atm, when $r_A \geq r_{\text{Nd}^{3+}}$ the perovskite-like structure forms, while when $r_A \leq r_{\text{Sm}^{3+}}$ the pyrochlore structure forms. Both structures are stable at high temperatures, with melting points occurring for all lanthanide compounds between 1600°C and 2000°C (Shcherbakova *et al.*, 1979; Teterin *et al.*, 1988), leading to a range of engineering applications.

The rare earth di-titanates in the perovskite-like structure have been shown to possess piezoelectric characteristics with high Curie temperatures, T_C , leading to many studies on high temperature piezoelectric properties (Turner *et al.*, 1994; Yan *et al.*, 2009; Sayir *et al.*, 2006). Many applications of these high-temperature piezoelectric sensors have been found for aerospace, automotive and power generation industries (Turner *et al.*, 1994). These materials also have high-temperature ferroelectric properties (Nanamatsu *et al.*, 1974; Kimura *et al.*, 1974; Gao *et al.*, 2013, 2016). Additionally, $\text{La}_2\text{Ti}_2\text{O}_7$ has photo-



catalytic properties with use in water-splitting reactions (Hwang *et al.*, 2003).

The $R_2\text{Ti}_2\text{O}_7$ pyrochlore structure is well known from studies of magnetic monopoles in frustrated magnetic, spin ice states (Bramwell *et al.*, 2009; Bramwell & Gingras, 2001; Sosin *et al.*, 2005; Samarakoon *et al.*, 2020). These structures also show high ionic conductivity and have been investigated for use as oxygen electrodes and electrolytes in solid oxide fuel cells (Moon & Tuller, 1988; Farmer *et al.*, 2014; Subramanian *et al.*, 1983). $\text{Gd}_2\text{Ti}_2\text{O}_7$ has been shown to be a good candidate for low-temperature magnetic refrigeration (Sosin *et al.*, 2005). Furthermore, they have been studied for two applications involving nuclear materials: *i.e.* for radiation damage resistance (Park *et al.*, 2015; Lian *et al.*, 2003) and for containment of radioactive and actinide waste, due to their low leaching rate (Subramanian *et al.*, 1983).

While many high-temperature properties of the $R_2\text{Ti}_2\text{O}_7$ compounds have been measured, crystallographic studies have not achieved the same elevated temperatures required to explain some of the properties. There have been few thermal expansion studies of these materials, and none to a sufficiently high temperature to understand the thermal stresses and strains that would develop during processing and in many proposed applications. Material behavior in air is more representative of most engineering applications than other environments, therefore this study was conducted in air where possible. Many characterization methods are unable to accomplish this due to instrumental constraints: *i.e.* a vacuum is required in most microscopies, oxidation of instrument components can occur in air at high-temperatures, and in some cases, temperature is controlled with a flowing inert gas.

The over-arching goal of this work was to measure the thermal expansion of the rare earth di-titanates in air to a high precision. A temperature-dependent study of cubic and monoclinic $R_2\text{Ti}_2\text{O}_7$ structures was carried out with *in situ* synchrotron diffraction up to 1600°C. The phase transition in $\text{La}_2\text{Ti}_2\text{O}_7$ (monoclinic to orthorhombic) was also characterized by *in situ* powder X-ray diffraction (XRD) and neutron powder diffraction (NPD). The following subsections describe the crystal structures, introduce important structural considerations of the rare earth di-titanates with an emphasis on high temperatures, and explain how the thermal expansion tensor is calculated.

1.1. $R_2\text{Ti}_2\text{O}_7$ structures, where $R = \text{La–Nd}$

The larger rare earth elements, $R = \text{La, Pr, Nd and Ce}$, in $R_2\text{Ti}_2\text{O}_7$ (or $R_2\text{O}_3 \cdot 2\text{TiO}_2$) form the perovskite-type layered structure which is monoclinic, space group $P2_1$ (No. 4), $Z = 4$, at 25°C and 1 atm (Gasparin, 1975; Ishizawa *et al.*, 1982, 2013; Kesari *et al.*, 2016). $\text{La}_2\text{Ti}_2\text{O}_7$ undergoes a phase transition at high temperatures to an orthorhombic structure, space group $\text{Cmc}2_1$ (No. 36), $Z = 4$. It is unclear if Pr, Nd and Ce undergo similar transformations. A transformation in $\text{La}_2\text{Ti}_2\text{O}_7$ at high pressure has been described in a preceding study (Zhang *et al.*, 2007).

There have been several structural studies of the monoclinic and orthorhombic rare earth di-titanate structures. One X-ray study (Ishizawa *et al.*, 1982) of single crystal $\text{La}_2\text{Ti}_2\text{O}_7$ found the $P2_1$ to $\text{Cmc}2_1$ transition to occur between 720°C and 780°C. Later, in electron diffraction (ED) and single crystal XRD studies, an incommensurately modulated phase was identified between the monoclinic and orthorhombic $\text{La}_2\text{Ti}_2\text{O}_7$ phases (Tanaka *et al.*, 1985; Ohi *et al.*, 1992; Ishizawa *et al.*, 2019). Recently, the structure of this incommensurately modulated phase and the associated phase transitions were described in detail, and reported to be present from 716°C to 807°C (Ishizawa *et al.*, 2019). $\text{Pr}_2\text{Ti}_2\text{O}_7$, $\text{Nd}_2\text{Ti}_2\text{O}_7$ and $\text{La}_2\text{Ti}_2\text{O}_7$ form the $P2_1$ structure at 25°C and 1 atm, so some have assumed that $\text{Pr}_2\text{Ti}_2\text{O}_7$ and $\text{Nd}_2\text{Ti}_2\text{O}_7$ have a phase transition to $\text{Cmc}2_1$ like $\text{La}_2\text{Ti}_2\text{O}_7$, however this phase transition has not been identified in $\text{Pr}_2\text{Ti}_2\text{O}_7$ between 25°C and 1200°C (Patwe *et al.*, 2015; Kesari *et al.*, 2016).

Some of the highest T_C have been measured in the La, Pr, and Nd di-titanates. These are reported to occur at a ferroelectric to paraelectric phase transition for $\text{La}_2\text{Ti}_2\text{O}_7$ and $\text{Nd}_2\text{Ti}_2\text{O}_7$ at over 1400°C and for $\text{Pr}_2\text{Ti}_2\text{O}_7$ at over 1500°C (Gasparin, 1975; Gao *et al.*, 2013, 2016; Patwe *et al.*, 2015). A corresponding structural transformation is expected, but it has not been experimentally measured. A paraelectric transformation to $P2_1/m$ on heating is predicted by Density Functional Theory (DFT) in $\text{Pr}_2\text{Ti}_2\text{O}_7$ (Patwe *et al.*, 2015).

There are few structural studies of $\text{Ce}_2\text{Ti}_2\text{O}_7$ because of its instability in air (due to the preference for the Ce^{4+} oxidation state instead of R^{3+} for $R = \text{La, Pr, and Nd}$) (Preuss & Gruehn, 1994; Gao *et al.*, 2015). For this reason, $\text{Ce}_2\text{Ti}_2\text{O}_7$ was also excluded here, as this study probed all compounds in air where possible, at atmospheric pressure.

1.2. $R_2\text{Ti}_2\text{O}_7$ structures, where $R = \text{Sm–Lu, Y}$

The smaller rare-earth elements, $R = \text{Sm through Lu, and Y}$, in $R_2\text{O}_3 \cdot 2\text{TiO}_2$ form the pyrochlore structure (cubic, space group $Fd\bar{3}m$, No. 227), $Z = 8$, at ambient conditions. This is a superstructure derivative of the fluorite structure (cubic, space group $Fm\bar{3}m$, No. 225). At atmospheric pressure, most studies have not measured a phase change up to melting.

One study (Shlyakhtina *et al.*, 2004) reported phase transformations in a subset of the cubic rare earth di-titanates, including the smaller rare earth cations: $\text{Lu}_2\text{Ti}_2\text{O}_7$, $\text{Yb}_2\text{Ti}_2\text{O}_7$, and $\text{Tm}_2\text{Ti}_2\text{O}_7$. They were reported to undergo a fluorite to pyrochlore-type phase transition on heating at 800°C, then a pyrochlore to fluorite-type phase transition near 1700°C in an *ex situ* X-ray study. While this is an unusual set of transformations, there are other reports of rare earth compounds going from low symmetry to high symmetry on cooling (Boulesteix, 1982). There are also a few reports of transformations at high pressures and temperatures (Agafonov *et al.*, 1979; Bondarenko *et al.*, 1998; Gao *et al.*, 2018).

The thermal expansion properties were measured for all the rare earth cubic pyrochlore structures (Sm–Lu and Y) (Farmer *et al.*, 2014), in which *in situ* powder X-ray diffraction studies in air up to 1000°C were carried out, but only reported a single

thermal expansion value over that range. The coefficients of thermal expansion of $\text{Gd}_2\text{Ti}_2\text{O}_7$ was also measured in another study from 25°C to 1200°C (Liu *et al.*, 2009). A few other studies give unit-cell parameters at elevated temperatures of a subset of $R_2\text{Ti}_2\text{O}_7$ (Ross *et al.*, 2012; Baroudi *et al.*, 2015). There have been several studies of ionic conductivity of the $R_2\text{Ti}_2\text{O}_7$ pyrochlores (van Dijk *et al.*, 1984; Wuensch *et al.*, 2000; Shlyakhtina *et al.*, 2008; Shlyakhtina & Shcherbakova, 2012; Nakamura *et al.*, 2016; Uno *et al.*, 2018). The thermal expansion and ionic conductivity of the isostructural $R_2\text{Zr}_2\text{O}_7$ pyrochlores have also been measured (Moriga *et al.*, 1989; Yamamura *et al.*, 2003; Hagiwara *et al.*, 2011, 2017). The present study aims to improve on these works by looking at a wider temperature range and calculating temperature-dependent coefficients of thermal expansion.

1.3. Thermal expansion

A complete description of the three-dimensional thermal expansion of lower symmetry crystalline materials is given by the second rank thermal expansion tensor, α_{ij} , which relates the change in strain tensor, $d\epsilon_{ij}$, to the change in temperature, dT , by $d\epsilon_{ij} = \alpha_{ij}dT$. This second rank tensor can be written symmetrically with six unique components, called coefficients of thermal expansion (CTE), in the lowest symmetry case. Crystallographic unit-cell vectors, **a**, **b** and **c**, will be related with Cartesian axis directions \hat{x} , \hat{y} , and \hat{z} , such that $\mathbf{c} \times \hat{z} = 0$, $\mathbf{b} \times \hat{y} = 0$, $\mathbf{a}^* \times \hat{x} = 0$, where $\mathbf{a}^* = \mathbf{b} \times \mathbf{c}$.

The calculation of the thermal expansion tensor, α_{ij} , involves (i) determining the unit-cell parameters via Rietveld refinement of powder diffraction data, (ii) the least-squares fitting of each to a function of temperature, (iii) the calculation of the temperature-dependent thermal expansion tensor via the set of equations in equation (1) (Schlenker *et al.*, 1975). Equations corresponding to the triclinic unit cell case can be found elsewhere (Paufler & Weber, 1999). Calculation of α_{ij} can be carried out in several different ways as described in Section S2. Eigenvalues, λ_i , of the thermal expansion tensor give the maximum and minimum values of thermal expansion in the direction given by the corresponding eigenvector.

$$\begin{aligned}\alpha_{11}(T) &= \frac{1}{a(T)} \frac{da(T)}{dT} + \cot \beta(T) \frac{d\beta(T)}{dT} \\ \alpha_{22}(T) &= \frac{1}{b(T)} \frac{db(T)}{dT} \\ \alpha_{33}(T) &= \frac{1}{c(T)} \frac{dc(T)}{dT} \\ \alpha_{13}(T) &= \frac{\cot \beta(T)}{2} \left[\frac{1}{a(T)} \frac{da(T)}{dT} - \frac{1}{c(T)} \frac{dc(T)}{dT} \right] - \frac{1}{2} \frac{d\beta(T)}{dT}\end{aligned}\quad (1)$$

Equation (1) is the calculation of the Eulerian α_{ij} tensor components from unit-cell parameter polynomials for monoclinic crystal systems.

2. Experimental

2.1. Powder synthesis

A sub-set of rare earth di-titanates, $R_2\text{Ti}_2\text{O}_7$, was synthesized, where $R = \text{La, Pr, Nd, Sm, Gd, Dy, Er, Yb, and Y}$. These were chosen because they make up a wide range of cation sizes in this period. Powder samples were synthesized using a solution-based ceramic powder synthesis method called the organic inorganic steric entrapment method (Seymour *et al.*, 2016, 2015; Gülgün *et al.*, 1999, 2002; Nguyen *et al.*, 1999), depicted by the flow chart and additional details in Section S3.1. This presents a new synthesis route for the rare earth di-titanates at a lower temperature than several other methods (Fuierer & Newnham, 1991). Successful single-phase synthesis of each powder sample was confirmed by laboratory X-ray diffraction (XRD), with a description in Section S3.2.

2.2. High-temperature synchrotron and neutron powder diffraction

Each rare earth di-titanate powder was mixed with 5–10 wt% Pt powder (99.9%, Sigma Aldrich, Milwaukee, WI) which served as an internal temperature standard and as a thermal conductor, ensuring homogeneous heating and absorption of the infrared light from the optical furnace during synchrotron experiments. Thermal expansion of Pt (Touloukian, 1975) was used to calculate the temperature of the sample. Powder samples were mounted in sapphire capillaries (single crystal, grown down *c*-axis, 0.6 mm ID \times 1 mm OD, Crytur, Turnov, Czech Republic) and held at the end of an alumina tube (1.1 mm ID, 1.7 mm OD, Alfa Aesar, Ward Hill, MA, USA). Each sample was rotated in the goniometer of the diffractometer.

High-temperature X-ray diffraction (XRD) was used to characterize the rare earth di-titanate samples in air in transmission geometry. Data was collected at the 33 BM-C beamline at the Advanced Photon Source (APS) at Argonne National Laboratory (ANL) (Lemont, IL, USA). The wavelength of 0.590083 Å at APS was calculated from a powder LaB_6 standard. Data was also collected at the 28 ID-2 beamline at the National Synchrotron Light Source II (NSLS II) at Brookhaven National Laboratory (BNL) (Upton, NY, USA) at a wavelength of 0.236996 Å. A quadrupole lamp furnace (QLF) mounted at each beamline heated samples from temperature up to 1600°C (Sarin *et al.*, 2006). Data was acquired in the range between inverse *d*-spacing of about 0.12 Å^{−1} and 1.0 Å^{−1} using a Pilatus 100 K detector at APS and a 16'' \times 16'' flat scintillator detector at NSLS II.

When possible, and prior to azimuthal image integration of the reflection intensities, masks were applied using the program *General Structure Analysis System* (GSAS II) (Toby & Von Dreele, 2013) to remove the Bragg peaks of the single crystal sapphire capillaries. The Rietveld method (Rietveld, 1969) was used to refine XRD patterns with $Fd\bar{3}m$, $P2_1$ or $Cmc2_1$ $R_2\text{Ti}_2\text{O}_7$ structures (Farmer *et al.*, 2014; Ishizawa *et al.*, 1982, 2013) by means of the Bruker *TOPAS* software (Perl *et al.*, 2012). Each phase present in a sample was refined for scale,

unit-cell parameters, and atomic positions of the rare earth element and titanium.

Neutron powder diffraction (NPD) data was collected for $\text{La}_2\text{Ti}_2\text{O}_7$, $\text{Nd}_2\text{Ti}_2\text{O}_7$ and $\text{Pr}_2\text{Ti}_2\text{O}_7$, in vacuum at the POWGEN beamline 11 A at the Spallation Neutron Source at Oak Ridge National Laboratory (Oak Ridge, TN, USA). Temperatures up to 1200°C were reached with the MICAS generation II vacuum furnace. This time-of-flight neutron diffraction data was collected in the range between inverse d -spacing of about 0.0769 Å⁻¹ and 2.06 Å⁻¹ (center wavelength of 1.5 Å⁻¹). NPD data were analyzed with the Rietveld method in the range between 0.188 Å⁻¹ and 1.614 Å⁻¹, chosen where the data was least noisy, in the Bruker (2011) *TOPAS*

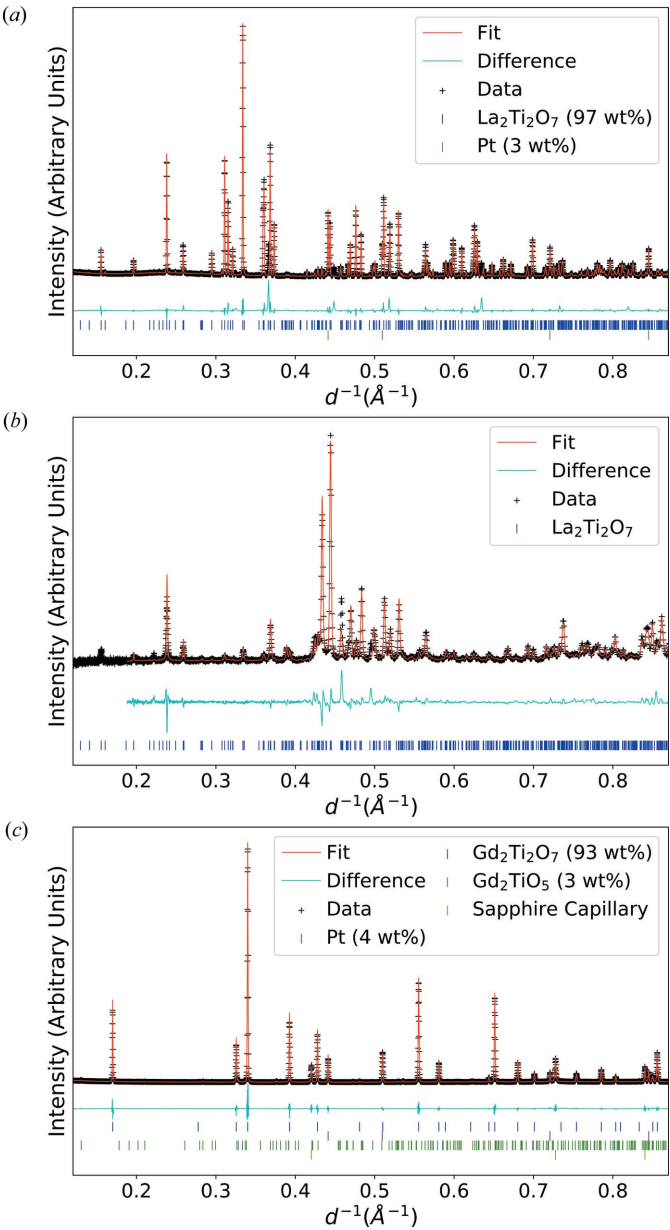


Figure 1
Powder diffraction patterns collected at 25°C for (a) X-ray and (b) neutron diffraction of $\text{La}_2\text{Ti}_2\text{O}_7$ in the monoclinic $P2_1$ space group and (c) X-ray diffraction of $\text{Gd}_2\text{Ti}_2\text{O}_7$ in the cubic $Fd\bar{3}m$ space group. Pt peaks are from the internal temperature standard.

Table 1
Crystallographic and Rietveld data for select $R_2\text{Ti}_2\text{O}_7$.

	$\text{La}_2\text{Ti}_2\text{O}_7$	$\text{La}_2\text{Ti}_2\text{O}_7$	$\text{Gd}_2\text{Ti}_2\text{O}_7$
Crystal data			
Crystal system	Monoclinic	Monoclinic	Cubic
Space group	$P2_1$ (No. 4)	$P2_1$ (No. 4)	$Fd\bar{3}m$ (No. 227)
Z	4	4	8
T (°C)	25.1 (8.2)	32.2	25.0 (1.6)
a (Å)	7.82032 (11)	7.8135 (2)	10.184640 (19)
b (Å)	5.54432 (8)	5.54320 (17)	10.184640 (19)
c (Å)	13.0049 (2)	13.0089 (5)	10.184640 (19)
α, β, γ (°)	90, 98.662 (4), 90	90, 98.660 (9), 90	90, 90, 90
V (Å ³)	557.438 (16)	557.01 (4)	1056.421 (6)
Data collection			
Radiation type	X-ray	Neutron	X-ray
Diffractometer	33 BM-C	BL-11A POWGEN	33 BM-C
Source, laboratory	APS, ANL	SNS, ORNL	APS, ANL
λ (Å)	0.590183756	-	0.590183756
d^{-1}_{min} (Å ⁻¹)	0.12	0.19	0.12
d^{-1}_{max} (Å ⁻¹)	0.88	1.61	0.99
Atmosphere	Air	Vacuum	Air
Sample container	Fused-silica capillary	Vanadium canister	Sapphire capillary
Rietveld refinement			
Computer program	<i>TOPAS</i>	<i>TOPAS</i> with <i>Topas_Highres.inp</i> for 2018-B	<i>TOPAS</i>
Wt% - Rietveld†	96.82 (5)	100	93.43 (8)
R_{wp} (%)‡	13.4	1.27	9.37
R_{exp} (%)‡	31.55	0.50	1.34
R_p (%)‡	6.97	1.14	6.6
GoF (%)‡	0.42	2.51	7
R_{Bragg} ‡	5.61	6.72	2.14

† Remaining wt% from Pt or minor phases. ‡ Values are as defined in *TOPAS* v5 (Bruker, 2011).

software (with *Topas_Highres.inp*, found on the POWGEN user website for cycle 2018-B). Each phase present in a sample was refined for scale, unit-cell parameters, atomic positions of all atoms, as well as their displacement parameters.

3. Results and discussion

Representative room-temperature synchrotron and neutron diffraction patterns for $\text{La}_2\text{Ti}_2\text{O}_7$ in space group $P2_1$ and for $\text{Gd}_2\text{Ti}_2\text{O}_7$ in space group $Fd\bar{3}m$ are shown in Fig. 1 with crystallographic, Rietveld and data collection information given in Table 1. Additional data are given in the Tables S4, S5 and S6. Structural results of Rietveld refinements for both space groups agree with past published data (Farmer *et al.*, 2014; Ishizawa *et al.*, 1982, 2013).

3.1. Cubic ($Fd\bar{3}m$) thermal expansion

The temperature-dependent unit-cell dimensions for the cubic samples are seen in Fig. 2(a) for the temperature range: 25°C–1600°C. Second-order polynomial fit of unit-cell parameters and the calculated thermal expansion coefficients are seen in Fig. 2(b) and Table 2. Error bars are smaller than the data markers. All samples show a positive isotropic thermal expansion coefficient of $9 \times 10^{-6} \text{ °C}^{-1}$ to $13 \times 10^{-6} \text{ °C}^{-1}$. As

Table 2

Polynomial fits of X-ray-derived unit-cell parameter and coefficient of thermal expansion for the cubic rare-earth di-titanates.

	Sm ₂ Ti ₂ O ₇	Gd ₂ Ti ₂ O ₇	Dy ₂ Ti ₂ O ₇	Er ₂ Ti ₂ O ₇	Yb ₂ Ti ₂ O ₇	Y ₂ Ti ₂ O ₇
T_{\min} (°C)	25	25	25	25	25	25
T_{\max} (°C)	1561	1534	1516	1544	1550	1597
a (Å)						
A_0	10.2304 (5)	10.1829 (11)	10.1212 (8)	10.0794 (15)	10.0216 (17)	10.0959 (12)
A_1	$8.52 (12) \times 10^{-5}$	$9.5 (3) \times 10^{-5}$	$1.01 (2) \times 10^{-4}$	$9.8 (4) \times 10^{-5}$	$1.11 (4) \times 10^{-4}$	$9.3 (3) \times 10^{-5}$
A_2	$1.65 (7) \times 10^{-8}$	$1.22 (17) \times 10^{-8}$	$7.2 (1.3) \times 10^{-9}$	$9.2 (2.6) \times 10^{-9}$	$-2.4 (2.6) \times 10^{-10}$	$1.33 (19) \times 10^{-8}$
α_{11} (°C ⁻¹)						
A_0	$8.436 (2) \times 10^{-6}$	$9.4411 (17) \times 10^{-6}$	$1.00141 (11) \times 10^{-5}$	$9.6474 (14) \times 10^{-6}$	$1.09818 (3) \times 10^{-5}$	$9.242 (18) \times 10^{-6}$
A_1	$3.108 (3) \times 10^{-9}$	$2.2698 (19) \times 10^{-9}$	$1.281 (12) \times 10^{-9}$	$1.6879 (16) \times 10^{-9}$	$-1.676 (3) \times 10^{-10}$	$2.3584 (19) \times 10^{-9}$

anticipated, there was a relationship between unit-cell parameters and cation size, with the larger cations having larger unit-cell parameters. There was not a clear relationship between thermal expansion coefficient and cation size from temperature to 1600°C, however. Tabulated temperature-dependent unit-cell parameter values including estimate standard uncertainties (s.u.'s) determined from Rietveld refinement analysis can be found in Section S4.

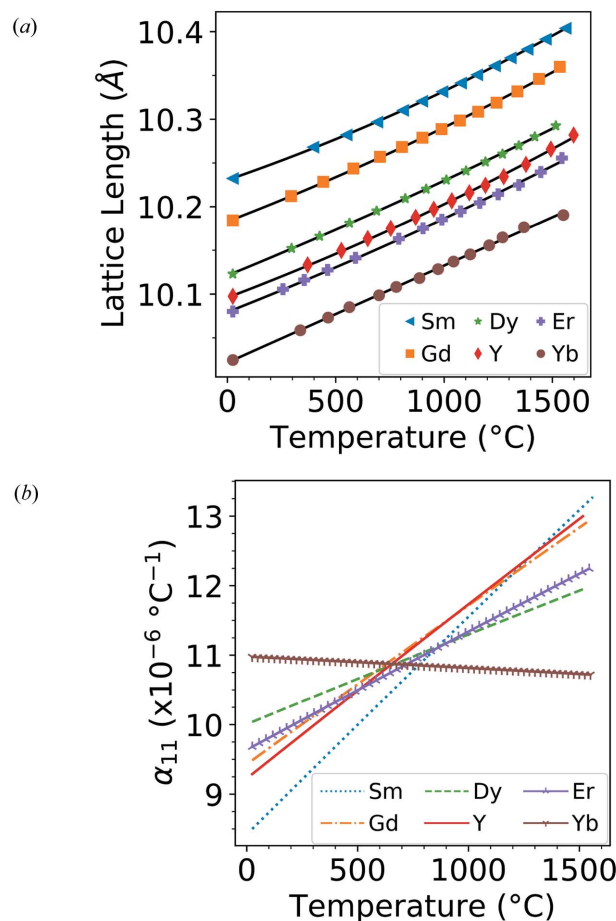


Figure 2

(a) Unit-cell constants and polynomial fit for the cubic pyrochlore compounds, $R_2Ti_2O_7$, where $R = Sm, Gd, Dy, Y, Er$ and Yb . Error bars are smaller than the data markers. (b) The corresponding thermal expansion coefficients.

3.2. Monoclinic ($P2_1$) and orthorhombic ($Cmc2_1$) thermal expansion

Three unit-cell parameters and the β angle are required to describe the unit cell of the monoclinic rare earth di-titanates, and these values are given for the samples at temperatures between 25°C and ~1400°C in Fig. 3. Error bars are smaller than the data markers. Analysis of each sample involved the fitting of a second-order polynomial to strain tensor components. The four components of the thermal expansion tensor needed to fully describe its three-dimensional expansion were calculated and are summarized in Fig. 4 and Table 3. This presents the first thermal expansion tensor of monoclinic and

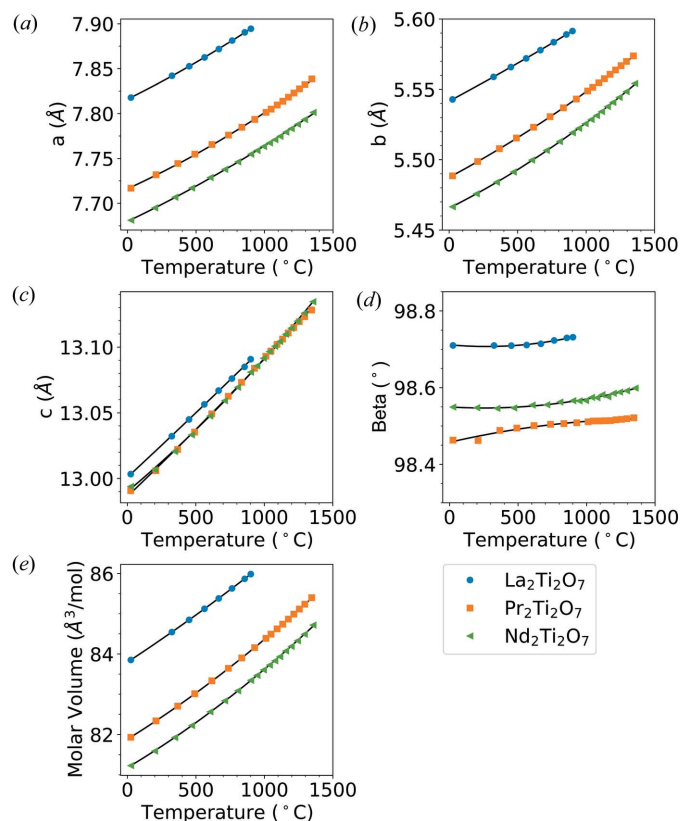


Figure 3

Unit-cell parameters (a), (b), (c), β -angles (d) and molar volumes (e) as functions of temperature for the monoclinic structures of $La_2Ti_2O_7$, $Pr_2Ti_2O_7$ and $Nd_2Ti_2O_7$ derived from XRD data. Error bars are smaller than the data markers.

Table 3
Crystal data and polynomial fit of unit-cell parameters and α_{ij} components for $\text{La}_2\text{Ti}_2\text{O}_7$, $\text{Pr}_2\text{Ti}_2\text{O}_7$ and $\text{Nd}_2\text{Ti}_2\text{O}_7$ samples from XRD data.

	$\text{La}_2\text{Ti}_2\text{O}_7$	$\text{La}_2\text{Ti}_2\text{O}_7$	$\text{Pr}_2\text{Ti}_2\text{O}_7$	$\text{Nd}_2\text{Ti}_2\text{O}_7$
T_{\min} ($^{\circ}\text{C}$)	25	885	25	25
T_{\max} ($^{\circ}\text{C}$)	885	1530	1345	1456
Unit-cell parameter: a (\AA)			$a(T) = A_0 + A_1T + A_2T^2$	
A_0	7.8160 (3)	3.918 (4)	7.7164 (5)	7.684 (3)
A_1	$7.53 (15) \times 10^{-5}$	$2.37 (6) \times 10^{-5}$	$7.03 (14) \times 10^{-5}$	$5.1 (9) \times 10^{-5}$
A_2	$1.34 (15) \times 10^{-8}$	$9.3 (2.4) \times 10^{-9}$	$1.4 (1) \times 10^{-8}$	$2.9 (6) \times 10^{-8}$
Unit-cell parameter: b (\AA)			$b(T) = A_0 + A_1T + A_2T^2$	
A_0	5.54156 (9)	25.74 (6)	5.4878 (2)	5.468 (2)
A_1	$5.24 (4) \times 10^{-5}$	$-1.4 (9.7) \times 10^{-5}$	$5.17 (7) \times 10^{-5}$	$3.4 (6) \times 10^{-5}$
A_2	$3.3 (4) \times 10^{-9}$	$1.9 (4) \times 10^{-7}$	$9.0 (5) \times 10^{-9}$	$2.4 (4) \times 10^{-8}$
Unit-cell parameter: c (\AA)			$c(T) = A_0 + A_1T + A_2T^2$	
A_0	13.0008 (7)	5.553 (5)	12.9866 (6)	12.992 (2)
A_1	$9.7 (3) \times 10^{-5}$	$3.0 (9) \times 10^{-5}$	$9.9 (2) \times 10^{-5}$	$7.4 (6) \times 10^{-5}$
A_2	$2.7 (3.0) \times 10^{-9}$	$1.5 (4) \times 10^{-8}$	$5.7 (1.3) \times 10^{-9}$	$2.5 (4) \times 10^{-8}$
Unit-cell parameter: β ($^{\circ}$)			$\beta(T) = A_0 + A_1T + A_2T^2$	
A_0	98.712 (3)	90.000	98.459 (2)	98.554 (4)
A_1	$-3.3 (1.1) \times 10^{-5}$	–	$7.7 (6) \times 10^{-5}$	$-4.2(1.1) \times 10^{-5}$
A_2	$6.2 (1.1) \times 10^{-8}$	–	$-2.5 (4) \times 10^{-8}$	$5.9 (7) \times 10^{-8}$
α_{11} ($^{\circ}\text{C}^{-1}$)			$\alpha_{11}(T) = A_0 + A_1T$	
A_0	$9.725 (3) \times 10^{-6}$	$6.051 (3) \times 10^{-6}$	$8.936 (6) \times 10^{-6}$	$6.8 (2) \times 10^{-6}$
A_1	$2.956 (6) \times 10^{-9}$	$4.664 (6) \times 10^{-9}$	$3.704 (7) \times 10^{-9}$	$7.12 (2) \times 10^{-9}$
α_{22} ($^{\circ}\text{C}^{-1}$)			$\alpha_{22}(T) = A_0 + A_1T$	
A_0	$9.4649 (9) \times 10^{-6}$	$-5.46 (7) \times 10^{-7}$	$9.439 (5) \times 10^{-6}$	$6.229 (17) \times 10^{-6}$
A_1	$1.0972 (17) \times 10^{-9}$	$1.4337 (13) \times 10^{-8}$	$3.114 (6) \times 10^{-9}$	$8.61 (2) \times 10^{-9}$
α_{33} ($^{\circ}\text{C}^{-1}$)			$\alpha_{33}(T) = A_0 + A_1T$	
A_0	$4.0341 (2) \times 10^{-6}$	$-2.52 (3) \times 10^{-6}$	$3.9855 (12) \times 10^{-6}$	$2.61 (4) \times 10^{-6}$
A_1	$4.782 (5) \times 10^{-10}$	$6.63 (6) \times 10^{-8}$	$1.3356 (15) \times 10^{-9}$	$3.655 (5) \times 10^{-9}$
α_{13} ($^{\circ}\text{C}^{-1}$)			$\alpha_{13}(T) = A_0 + A_1T$	
A_0	$-1.3759 (3) \times 10^{-7}$	–	$-1.0506 (4) \times 10^{-6}$	$6.34 (2) \times 10^{-8}$
A_1	$-1.29219 (5) \times 10^{-9}$	–	$2.618 (5) \times 10^{-10}$	$-1.321 (2) \times 10^{-9}$

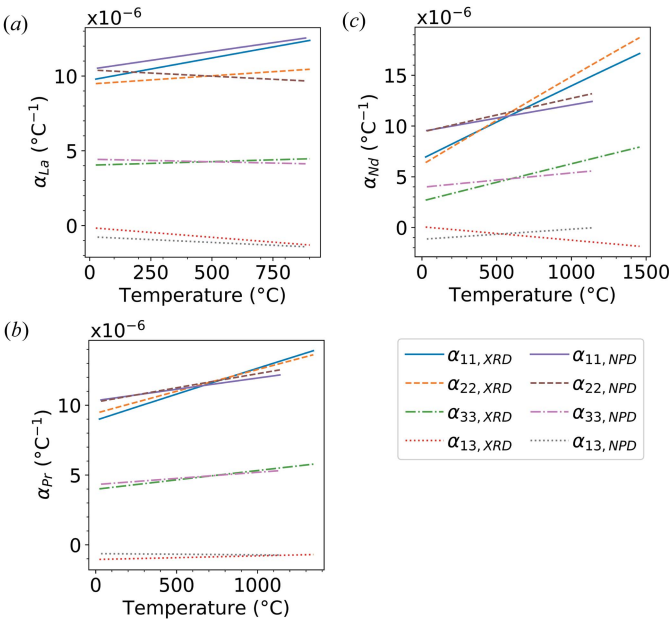


Figure 4
Components of the thermal expansion tensor, α_{11} , α_{22} , α_{33} and α_{13} , as functions of temperature for the monoclinic samples (a) $\text{La}_2\text{Ti}_2\text{O}_7$, (b) $\text{Pr}_2\text{Ti}_2\text{O}_7$, and (c) $\text{Nd}_2\text{Ti}_2\text{O}_7$ from both XRD and NPD experiments.

orthorhombic rare earth di-titanates, as there are no prior thermal expansion studies with which to compare these results. The three-dimensional thermal expansion tensor can be visualized as a quadric surface, and example quadric surfaces are shown in Fig. 5. All monoclinic samples have similar CTE values and trends between components of α_{ij} , α_{11} , α_{22} and α_{33} are all positive CTE values, between $5 \times 10^{-6} \text{C}^{-1}$ and $17 \times 10^{-6} \text{C}^{-1}$. α_{13} is near zero or slightly negative. There

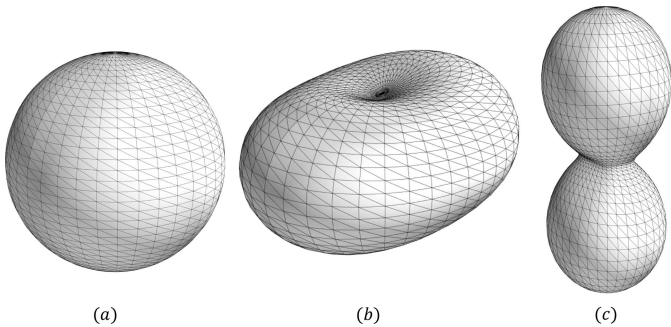


Figure 5
Representative quadric surfaces of the three-dimensional thermal expansion tensors for (a) cubic, (b) monoclinic and (c) orthorhombic $\text{R}_2\text{Ti}_2\text{O}_7$.

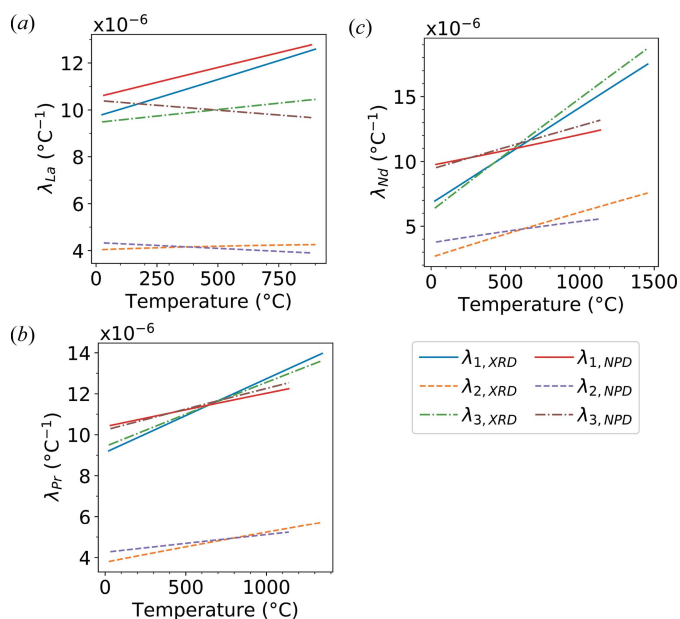


Figure 6
Eigenvalues of the thermal expansion tensor, λ_1 , λ_2 , λ_3 , as functions of temperature for the monoclinic samples (a) $\text{La}_2\text{Ti}_2\text{O}_7$, (b) $\text{Pr}_2\text{Ti}_2\text{O}_7$, and (c) $\text{Nd}_2\text{Ti}_2\text{O}_7$ from both XRD and NPD experiments.

is good agreement in CTE values derived from XRD and NPD experiments.

The anisotropy in the thermal expansion of monoclinic $\text{La}_2\text{Ti}_2\text{O}_7$, $\text{Pr}_2\text{Ti}_2\text{O}_7$, and $\text{Nd}_2\text{Ti}_2\text{O}_7$ can be compared by inspection of the eigenvalues, λ_i , of the thermal expansion tensor, α_{ij} . For orthorhombic $\text{La}_2\text{Ti}_2\text{O}_7$, the eigenvalues are

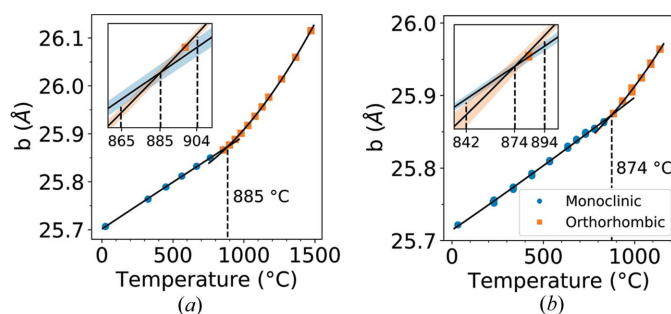


Figure 7
The $\text{La}_2\text{Ti}_2\text{O}_7$ b unit-cell parameter as a function of temperature determined from (a) XRD and (b) NPD data both shown in the orthorhombic basis. Error bars for data points are smaller than the markers. This most clearly displays the change in unit-cell parameter value at the monoclinic to orthorhombic transformation. The transformation temperature in (a) XRD is 885°C (864°C – 904°C) and in (b) NPD is 874°C (841°C – 894°C) which occurs at the intersection of each quadratic fit. The shaded regions show one standard deviation from the second-order polynomial regressions and are a measure of the uncertainty in this intersection.

simply equal to the components of α_{ij} , when $i = j$. The eigenvalues for the monoclinic $\text{La}_2\text{Ti}_2\text{O}_7$, $\text{Pr}_2\text{Ti}_2\text{O}_7$ and $\text{Nd}_2\text{Ti}_2\text{O}_7$ are shown in Fig. 6. All three samples show similar anisotropy, each with the lowest thermal expansion for λ_2 . For the standard setting of the unit cell used here (defined in §1.3), the b -axis is aligned with the eigenvector for λ_2 , and the eigenvectors for λ_1 and λ_3 give directions in the a - c plane.

Monoclinic $R_2\text{Ti}_2\text{O}_7$ unit-cell diagrams show that the b -axis includes a single perovskite layer, whereas the a and c -axes include two perovskite layers, as seen in Fig. S1. The minimum

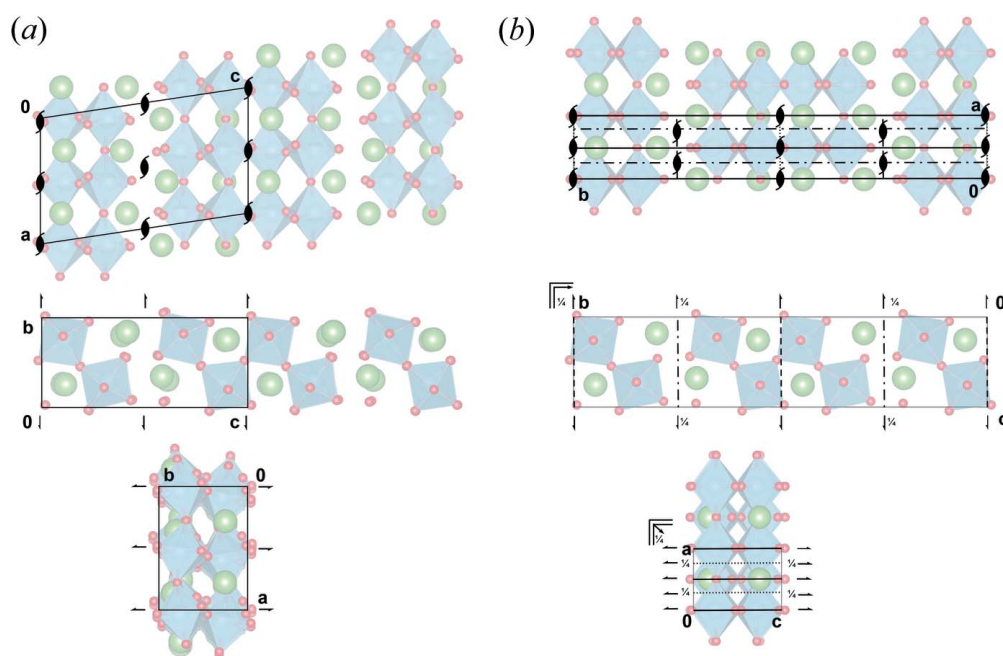


Figure 8
The structural changes of a $\text{La}_2\text{Ti}_2\text{O}_7$ unit cell or motif in going between the (a) low-temperature monoclinic (P_2) structure and the (b) high-temperature orthorhombic (Cmc_2) structure are described by the tilting and rotation of TiO_6 octahedra. Symmetry element diagrams superimposed on the unit cell with atomic positions are shown. Additional symmetry can be seen after the phase transformation to Cmc_2 . $Z = 4$ for both unit cells.

thermal expansion being in the b -axis direction suggests that the expansion is mainly caused by greater relative motion between the perovskite layers (only measured in the a - c plane by λ_1 and λ_3) than the expansion within a single layer (present in the a , b and c -axis directions).

Tabulated X-ray-derived and neutron-derived temperature-dependent unit-cell parameter values including standard uncertainties for monoclinic and orthorhombic structures can be found in Sections S5 and S6, respectively. NPD unit-cell parameter polynomials, α_{ij} component polynomials, and plots are found in Section S7. Plots of all orthorhombic $\text{La}_2\text{Ti}_2\text{O}_7$ unit-cell parameters, molar volume, α_{ij} components, and λ_i components are given in Section S6.

3.3. Monoclinic ($P2_1$) to orthorhombic ($Cmc2_1$) transformation

Phase transformations are generally determined in XRD by the change in relative intensity and/or position of Bragg peaks. In the change from monoclinic to orthorhombic $\text{La}_2\text{Ti}_2\text{O}_7$ there are several low intensity Bragg peaks that disappear, but the transformation occurs at a high temperature and these peaks are so small that it cannot be determined if the disappearance is due to a phase change or due to thermal effects like the Debye–Waller factor and temperature-diffuse scattering. For this reason, the transformation temperature was determined by the change in slope of the unit-cell parameters before and after the transformation.

The number of formula units per unit cell is 4 for both the monoclinic ($P2_1$) and orthorhombic ($Cmc2_1$) unit cells, making comparison of unit-cell volume relatively simple. The volume change between monoclinic and orthorhombic $\text{La}_2\text{Ti}_2\text{O}_7$ is approximately zero, $\Delta V = 0.005 \pm 0.007 \text{ \AA}^3$. However, the unit-cell parameters cannot be directly compared due to the differing unit cells. The c unit-cell parameter of the monoclinic phase was calculated for the corresponding b unit-cell parameter of the higher symmetry orthorhombic phase in Figs. 7(a) and 7(b) to facilitate comparison.

The X-ray atomic scattering factor for O is much lower than that of La or Ti, causing O positions to be easier to determine from neutron diffraction experiments (Henke *et al.*, 1993; Sears, 1992). This phase transition is measured better with the NPD experiments than powder XRD. Due to the similarity of the monoclinic and orthorhombic structures and the difficulty determining the transformation temperature from the Rietveld refinement, the change in the slope of the unit-cell parameters led to the precise determination of the $\text{La}_2\text{Ti}_2\text{O}_7$ transformation temperature. This was most easily seen by looking at the orthorhombic b unit-cell parameter, shown in Fig. 7. The intersection of two quadratic fits of either side of the transformation more accurately determined the transformation temperature than looking only at when a singular powder XRD pattern changed phase. The transformation temperature is 885°C with an uncertainty of 864–904°C for the XRD experiment and 874°C with an uncertainty of 841–894°C for the NPD experiment. The uncertainty in the transformation temperatures given here is determined by the intersection

of confidence limits for each least-squares regression polynomial that represent ± 1 standard deviation of the least-squares parameters from the regression line. This temperature range represents an overestimate in the uncertainty of the intersection (Carter *et al.*, 1991).

Neutron (in vacuum) and X-ray (in air) experiments showed slightly different temperature-dependent effects, as has been reported in related systems (Seymour *et al.*, 2015; Sinha & Sharma, 2005). The difference in transformation temperature could be caused by the differences in experimental atmosphere. Neutron experiments could only be carried out in vacuum at the required temperatures to prevent oxidation of the vanadium heating element (which is detrimental to the neutron transparent nature of vanadium). X-ray experiments were carried out in air, which is the operating condition for most applications. Oxygen vacancies that form in air upon heating affect thermal expansion (Taylor, 1998; Aidhy *et al.*, 2015), but the difference in oxygen vacancy formation in air versus in vacuum for the rare earth di-titanates (and their effect on thermal expansion) were outside the scope of this study. For this reason, neutron and X-ray data were refined separately, leading to separate X-ray and neutron-derived $\alpha_{ij}(T)$.

No phase transformation was observed in monoclinic $\text{Pr}_2\text{Ti}_2\text{O}_7$ and $\text{Nd}_2\text{Ti}_2\text{O}_7$ between 25°C and $\sim 1400^\circ\text{C}$, which is attributed to the size of the rare earth cation. This cation-size dependence on structure and transformation is in agreement with studies of other rare-earth compounds, as shown in the room-temperature phases of the rare earth di-titanates (Roth, 1956), the transformations of rare earth titanates (R_2TiO_5) (Seymour *et al.*, 2015), rare earth phosphates, arsenates, and vanadates (Carron *et al.*, 1958), as well as in rare earth niobates (Gingerich & Bair, 1963).

The additional symmetry in the orthorhombic structure are from c -centering and a c -glide perpendicular to b (Ishizawa *et al.*, 1982). This change in symmetry is achieved by a rotation of the TiO_6 octahedra, as seen in Fig. 8. The refined $\text{La}_2\text{Ti}_2\text{O}_7$ crystal structures here do not improve upon the recent single crystal phase transformation study describing the incommensurately modulated phase between the $P2_1$ and $Cmc2_1$ phases (Ishizawa *et al.*, 2019). The incommensurately modulated phase was not refined here due to the difficulty of discerning modulated structures from powder diffraction experiments (Zhou *et al.*, 2016). In the past, the incommensurately modulated phase was studied, in part, through twinned single crystals which is not possible in powder diffraction (Tanaka *et al.*, 1985; Ishizawa *et al.*, 2019). The description of the transformation here shows an alternative approach to measuring phase transformations with simpler synthesis (powder synthesis versus single crystal) and with faster, higher resolution characterization methods (synchrotron powder diffraction versus laboratory source single crystal). The unit-cell parameter and thermal expansion data derived from powder synchrotron and neutron source experiments here have higher resolution data over past single-crystal studies at laboratory X-ray sources. A comparison of three $\text{La}_2\text{Ti}_2\text{O}_7$ phase transformation studies with the present one is found in Section S9.

The movement of atoms before and after the transformation in $\text{La}_2\text{Ti}_2\text{O}_7$ is consistent with a displacive transformation due to the proximity of atoms in each phase (Buerger, 1951, 1948). There are interesting applications involving displacive transformations in ceramics (Hannink *et al.*, 2000; Kim & Kriven, 1998; Kriven, 1988), including transformation toughening and mechanical rearrangement of ferroelastic domains, each dependent on the nature of unit-cell volume change accompanying the displacive transformation (Kriven, 1995; Kriven & Lee, 1998, 2002, 2005). The use of $\text{La}_2\text{Ti}_2\text{O}_7$ for these applications would require further investigation.

The change of basis matrix (unit-cell variant deformation matrix) in equation (2), calculated with the program *Isodistort* (Campbell *et al.*, 2006; Stokes, Hatch & Campbell; <https://stokes.byu.edu/iso/isotropy.php>), describes the transformation in unit-cell vectors from monoclinic ($P2_1$) to orthorhombic ($Cmc2_1$) symmetry. If there were a large volume change on transformation determining the change of basis matrix is more complex, the relationship between phases could be determined with symmetry decomposition analysis involving continuous d_{hkl} values between phases, as demonstrated previously (McCormack *et al.*, 2018). Continuous d_{hkl} values for $\text{La}_2\text{Ti}_2\text{O}_7$ are given in Section S7. The symmetry relation here confirmed one described in the literature (Ishizawa *et al.*, 1982). Visualization of the group–subgroup relationship was found with the Bilbao Crystallographic Server (Ivantchev *et al.*, 2000; Aroyo, Perez-Mato *et al.*, 2006; Aroyo, Kirov *et al.*, 2006; Aroyo *et al.*, 2011) and can be found in Section S8.

$$\begin{bmatrix} \mathbf{a} \\ \mathbf{b} \\ \mathbf{c} \end{bmatrix}_{P2_1} = \begin{bmatrix} -2 & 0 & 0 \\ 0 & 0 & 1 \\ \frac{1}{2} & \frac{1}{2} & 0 \end{bmatrix} \begin{bmatrix} \mathbf{a} \\ \mathbf{b} \\ \mathbf{c} \end{bmatrix}_{Cmc2_1} \quad (2)$$

Equation (2) is change of basis matrix that describes the transformation in $\text{La}_2\text{Ti}_2\text{O}_7$ unit-cell vectors between $P2_1$ and $Cmc2_1$.

4. Conclusion

Accurate measurement of the thermal expansion tensors of the rare earth di-titanates is important for their use in most applications. A set of rare earth di-titanates, $R_2\text{Ti}_2\text{O}_7$ ($R = \text{La}, \text{Pr}, \text{Nd}, \text{Sm}, \text{Gd}, \text{Dy}, \text{Er}, \text{Yb}, \text{Y}$), were synthesized for the first time by the organic inorganic steric entrapment method. High-resolution, high-temperature synchrotron and neutron diffraction experiments led to the determination of novel temperature-dependent thermal expansion tensors for powder samples of rare earth di-titanates. This work elaborates on past research of the thermal expansion in the cubic rare earth di-titanates and presents the first calculation of the thermal expansion tensor of the monoclinic and orthorhombic rare earth di-titanates. The anisotropic thermal expansion of monoclinic $R_2\text{Ti}_2\text{O}_7$ was discussed and related to the perovskite-like layered crystal structure. The $\text{La}_2\text{Ti}_2\text{O}_7$ monoclinic to orthorhombic transformation temperature was measured in air with synchrotron powder XRD at 885°C and in vacuum with NPD at 874°C and compared with single-crystal studies.

This work showed a simpler approach to measuring this phase transformation temperature than previous single-crystal studies. It was shown that there is no transformation in $\text{Nd}_2\text{Ti}_2\text{O}_7$ and $\text{Pr}_2\text{Ti}_2\text{O}_7$ up to about 1500°C, thereby extending previous structural studies by almost 400°C.

5. Related literature

The following references are cited in the supporting information: Allen (1974); Ballirano & Melis (2009); Belousov & Filatov (2007); Belsky *et al.* (2002); Deshpande & Mudholker (1961); Garvie & Goss (1986); Herrera *et al.* (2013); Heuer *et al.* (1982); Huan *et al.* (2019); Jessen & Küppers (1991); Jones (2012); Jones *et al.* (2013); Kempter & Elliott (1959); Knight (1996); Knight *et al.* (1999); Küppers (2013); Langreiter & Kahlenberg (2015); Matthies & Wenk (2009); McCormack *et al.* (2020); Momma & Izumi (2008); Montgomery *et al.* (2012); Quan (1988); Saxena & Shen (1992); Schlenker *et al.* (1978); Toby (2006); Weber *et al.* (1998).

Acknowledgements

The technical assistance of beamline scientists Dr Evgenia Karapetrova at the APS, ANL, Dr Sanjit Ghose at NSLS II, BNL, Dr Ashfia Huq at the SNS, ORNL is gratefully acknowledged. The authors thank Gerard Mattei for helpful discussions about sequential Rietveld refinement. The authors declare no competing interests.

Funding information

The following funding is acknowledged: Air Force Office of Scientific Research (grant No. FA9550-15-1-0107 to Waltraud M. Kriven); National Science Foundation, Division of Materials Research (grant No. 1838595 to Waltraud M. Kriven). This research was carried out in part in the Frederick Seitz Materials Research Laboratory Central Facilities at the University of Illinois at Urbana-Champaign. Use of the Advanced Photon Source was supported by the U.S. Department of Energy, Office of Science, Office of Basic Energy Sciences, under Contract No. DE-AC02-06CH11357 and was completed at beamline 33 BM-C. This research used resources of beamline 28 ID-2 at the National Synchrotron Light Source II, a U.S. Department of Energy (DOE) Office of Science User Facility operated for the DOE Office of Science by Brookhaven National Laboratory under Contract No. DE-SC0012704. A portion of this research used resources at the Spallation Neutron Source, a DOE Office of Science User Facility operated by the Oak Ridge National Laboratory.

References

- Agafonov, V. N., Davydov, V. A., Porotnikov, N. V. & Petrov, K. I. (1979). *Russ. J. Inorg. Chem.* **24**, 1473–1477.
- Aidhy, D. S., Liu, B., Zhang, Y. & Weber, W. J. (2015). *Comput. Mater. Sci.* **99**, 298–305.
- Allen, D. M. (1974). *Technometrics*, **16**, 125–127.
- Aroyo, M. I., Kirov, A., Capillas, C., Perez-Mato, J. M. & Wondratschek, H. (2006). *Acta Cryst. A* **62**, 115–128.

- Aroyo, M. I., Perez-Mato, J. M., Capillas, C., Kroumova, E., Ivantchev, S., Madariaga, G., Kirov, A. & Wondratschek, H. (2006). *Z. Kristallogr.* **221**, 15–27.
- Aroyo, M. I., Perez-Mato, J. M., Orobengoa, D., Tasci, E., De La Flor, G. & Kirov, A. (2011). *Bulg. Chem. Commun.* **43**, 183–197. Crystallography Online: Bilbao Crystallographic Server.
- Ballirano, P. & Melis, E. (2009). *Phys. Chem. Miner.* **36**, 391–402.
- Baroudi, K., Gaulin, B. D., Lapidus, S. H., Gaudet, J. & Cava, R. J. (2015). *Phys. Rev. B*, **92**, 024110.
- Belousov, R. I. & Filatov, S. K. (2007). *Glass Phys. Chem.* **33**, 271–275.
- Belsky, A., Hellenbrandt, M., Karen, V. L. & Luksch, P. (2002). *Acta Cryst.* **B58**, 364–369.
- Bondarenko, T. N., Uvarov, V. N., Borisenko, S. V., Teterin, Y. A., Dzeghanovski, V. P., Sych, A. M. & Titiv, Y. A. (1998). *J. Korean Phys. Soc.* **32**, 65–67.
- Boulesteix, C. (1982). *Handbook on the Physics and Chemistry of Rare Earths*, Vol. 5, pp. 321–386. Elsevier.
- Bramwell, S. T., Giblin, S. R., Calder, S., Aldus, R., Prabhakaran, D. & Fennell, T. (2009). *Nature*, **461**, 956–959.
- Bramwell, S. T. & Gingras, M. J. P. (2001). *Science*, **294**, 1495–1501.
- Bruker (2011). *TOPAS*. Version 5. Bruker AXS, Karlsruhe, Germany.
- Buerger, M. J. (1948). *J. Miner. Soc. Am.* **33**, 101–121.
- Buerger, M. J. (1951). *Crystallographic Aspects of Phase Transformations. Proceedings of the Phase Transformations in Solids symposium*, held at Cornell University, August 23–26, 1948, edited by R. Smoluchowski, J. E. Mayer & W. A. Weyl, pp. 183–211. New York: Wiley.
- Campbell, B. J., Stokes, H. T., Tanner, D. E. & Hatch, D. M. (2006). *J. Appl. Cryst.* **39**, 607–614.
- Carron, M. K., Mrose, M. E. & Murata, K. J. (1958). *Am. Mineral.* **43**, 985–989.
- Carter, K. N., Scott, D. M., Salmon, J. K. & Zarcione, G. S. (1991). *Anal. Chem.* **63**, 1270–1278.
- Deshpande, V. T. & Mudholker, V. M. (1961). *Indian J. Phys.* **35**, 434–436.
- Farmer, J. M., Boatner, L. A., Chakoumakos, B. C., Du, M. H., Lance, M. J., Rawn, C. J. & Bryan, J. C. (2014). *J. Alloys Compd.* **605**, 63–70.
- Fuierer, P. A. & Newnham, R. E. (1991). *J. Am. Ceram. Soc.* **74**, 2876–2881.
- Gao, Z., Liu, L., Han, X., Meng, X., Cao, L., Ma, G., Liu, Y., Yang, J., Xie, Q. & He, H. (2015). *J. Am. Ceram. Soc.* **98**, 3930–3934.
- Gao, Z., Liu, Y., Lu, C., Xia, Y., Fang, L., Ma, Y., He, Q., He, D. & Yang, S. (2018). *J. Am. Ceram. Soc.* **101**, 2571–2577.
- Gao, Z., Lu, C., Wang, Y., Yang, S., Yu, Y. & He, H. (2016). *Sci. Rep.* **6**, 24139.
- Gao, Z. P., Yan, H. X., Ning, H. P. & Reece, M. J. (2013). *Adv. Appl. Ceram.* **112**, 69–74.
- Garvie, R. C. & Goss, M. F. (1986). *J. Mater. Sci.* **21**, 1253–1257.
- Gasparin, M. (1975). *Acta Cryst.* **B31**, 2129–2130.
- Schlenker, J. L., Gibbs, G. V. & Boisen, M. B. Jr (1978). *Acta Cryst.* **A34**, 52–54.
- Gingerich, K. A. & Bair, H. E. (1963). *Adv. X-ray Anal.* **7**, 22–30.
- Gülgin, M. A., Kriven, W. M. & Nguyen, M. H. (2002). US Patent number 6 482 387.
- Gülgin, M. A., Nguyen, M. H. & Kriven, W. M. (1999). *J. Am. Ceram. Soc.* **82**, 556–560.
- Hagiwara, T., Nomura, K. & Kageyama, H. (2017). *J. Ceram. Soc. Japan*, **125**, 65–70.
- Hagiwara, T., Yamamura, H. & Nishino, H. (2011). *IOP Conference Series: Materials Science and Engineering*, Vol. 18, p. 132003. IOP Publishing.
- Hannink, R. H. J., Kelly, P. M. & Muddle, B. C. (2000). *J. Am. Ceram. Soc.* **83**, 461–487.
- Henke, B. L., Gullikson, E. M. & Davis, J. C. (1993). *At. Data Nucl. Data Tables*, **54**, 181–342.
- Herrera, G., Jiménez-Mier, J. & Chavira, E. (2013). *Mater. Charact.* **89**, 13–22.
- Heuer, A. H., Claussen, N., Kriven, W. M. & Rühle, M. (1982). *J. Am. Ceram. Soc.* **65**, 642–650.
- Huan, L., Chenguang, L., Dongyan, Y., Yue, X. & Yuhong, L. (2019). *Nucl. Phys. Rev.* **36**, 248–255.
- Hwang, D. W., Lee, J. S., Li, W. & Oh, S. H. (2003). *J. Phys. Chem. B*, **107**, 4963–4970.
- Ishizawa, N., Marumo, F., Iwai, S., Kimura, M. & Kawamura, T. (1982). *Acta Cryst.* **B38**, 368–372.
- Ishizawa, N., Ninomiya, K., Sakakura, T. & Wang, J. (2013). *Acta Cryst.* **E69**, 19–19.
- Ishizawa, N., Ninomiya, K. & Wang, J. (2019). *Acta Cryst.* **B75**, 257–272.
- Ivantchev, S., Kroumova, E., Madariaga, G., Pérez-Mato, J. M. & Aroyo, M. I. (2000). *J. Appl. Cryst.* **33**, 1190–1191.
- Jessen, S. M. & Küppers, H. (1991). *J. Appl. Cryst.* **24**, 239–242.
- Jones, Z. A. (2012). MS Thesis, University of Illinois at Urbana-Champaign, USA.
- Jones, Z. A., Sarin, P., Haggerty, R. P. & Kriven, W. M. (2013). *J. Appl. Cryst.* **46**, 550–553.
- Kempter, C. P. & Elliott, R. O. (1959). *J. Chem. Phys.* **30**, 1524–1526.
- Kesari, S., Salke, N. P., Patwe, S. J., Achary, S. N., Sinha, A. K., Sastry, P. U., Tyagi, A. K. & Rao, R. (2016). *Inorg. Chem.* **55**, 11791–11800.
- Kim, Y. J. & Kriven, W. M. (1998). *J. Mater. Res.* **13**, 2920–2931.
- Kimura, M., Nanamatsu, S., Kawamura, T. & Matsushita, S. (1974). *Jpn. J. Appl. Phys.* **13**, 1473–1474.
- Knight, K. S. (1996). *Mineral. Mag.* **60**, 9.
- Knight, K. S., Stretton, I. C. & Schofield, P. F. (1999). *Phys. Chem. Miner.* **26**, 477–483.
- Kriven, W. M. (1988). *J. Am. Ceram. Soc.* **71**, 1021–1030.
- Kriven, W. M. (1995). *J. Phys. IV*, **5**, 101–110.
- Kriven, W. M. & Lee, S.-J. (1998). *Ceramic Engineering and Science Proceedings*, Vol. edited by D. Bray, pp. 305–316. John Wiley & Sons, Ltd.
- Kriven, W. M. & Lee, S.-J. (2002). US Patent number 6 361 888.
- Kriven, W. M. & Lee, S.-J. (2005). *J. Am. Ceram. Soc.* **88**, 1521–1528.
- Küppers, H. (2013). *International Tables for Crystallography*. Vol. D: Physical properties of crystals, pp. 100–105. Chichester: Wiley.
- Langreiter, T. & Kahlenberg, V. (2015). *Crystals*, **5**, 143–153.
- Lian, J., Chen, J., Wang, M., Ewing, R. C., Farmer, J. M., Boatner, L. A. & Helean, B. (2003). *Phys. Rev. B*, **68**, 134107.
- Liu, Z. G., Ouyang, J. H., Zhou, Y. & Xia, X. L. (2009). *Mater. Des.* **30**, 3784–3788.
- Matthies, S. & Wenk, H.-R. (2009). *J. Appl. Cryst.* **42**, 564–571.
- McCormack, S. J., Weber, R. J. & Kriven, W. M. (2018). *Acta Mater.* **161**, 127–137.
- McCormack, S. J., Wheeler, W. A., Hulbert, B. S. & Kriven, W. M. (2020). *Acta Mater.* **200**, 187–199.
- Momma, K. & Izumi, F. (2008). *J. Appl. Cryst.* **41**, 653–658.
- Montgomery, D., Peck, E. & Vining, G. (2012). *Introduction to Linear Regression Analysis*. Hoboken, New Jersey: John Wiley & Sons.
- Moon, P. K. & Tuller, H. L. (1988). *Solid State Ionics*, **28–30**, 470–474.
- Moriga, T., Yoshiasa, A., Kanamaru, F., Koto, K., Yoshimura, M. & Somya, S. (1989). *Solid State Ionics*, **31**, 319–328.
- Nakamura, K., Mori, M., Itoh, T. & Ohnuma, T. (2016). *AIP Adv.* **6**, 115003.
- Nanamatsu, S., Kimura, M., Doi, K., Matsushita, S. & Yamada, N. (1974). *Ferroelectrics*, **8**, 511–513.
- Nguyen, M. H., Lee, S. J. & Kriven, W. M. (1999). *J. Mater. Res.* **14**, 3417–3426.
- Ohi, K., Ishii, S. & Omura, H. (1992). *Ferroelectrics*, **137**, 133–138.
- Park, S., Lang, M., Tracy, C. L., Zhang, J., Zhang, F., Trautmann, C., Rodriguez, M. D., Kluth, P. & Ewing, R. C. (2015). *Acta Mater.* **93**, 1–11.
- Patwe, S. J., Katari, V., Salke, N. P., Deshpande, S. K., Rao, R., Gupta, M. K., Mittal, R., Achary, S. N. & Tyagi, A. K. (2015). *J. Mater. Chem. C*, **3**, 4570–4584.

- Paufler, P. & Weber, T. (1999). *Eur. J. Mineral.* **11**, 721–730.
- Perl, J., Shin, J., Schümann, J., Faddegon, B. & Paganetti, H. (2012). *Med. Phys.* **39**, 6818–6837.
- Preuss, A. & Gruehn, R. (1994). *J. Solid State Chem.* **110**, 363–369.
- Quan, N. T. (1988). *J. Bus. Econ. Stat.* **6**, 501–504.
- Rietveld, H. M. (1969). *J. Appl. Cryst.* **2**, 65–71.
- Ross, K. A., Proffen, T., Dabkowska, H. A., Quilliam, J. A., Yaraskavitch, L. R., Kycia, J. B. & Gaulin, B. D. (2012). *Phys. Rev. B*, **86**, 174424.
- Roth, R. S. (1956). *J. Res. Natl. Bur. Stand.* **56**, 17–25.
- Samarakoon, A. M., Barros, K., Li, Y. W., Eisenbach, M., Zhang, Q., Ye, F., Sharma, V., Dun, Z. L., Zhou, H., Grigera, S. A., Batista, C. D. & Tennant, D. A. (2020). *Nat. Commun.* **11**, 892.
- Sarin, P., Yoon, W., Jurkschat, K., Zschack, P. & Kriven, W. M. (2006). *Rev. Sci. Instrum.* **77**, 093906.
- Saxena, S. K. & Shen, G. (1992). *J. Geophys. Res.* **97**, 813–832.
- Sayir, A., Farmer, S. C. & Dynys, F. (2006). *Proceedings of the 107th Annual Meeting of The American Ceramic Society, Baltimore, Maryland, USA 2005*, pp. 57–68. John Wiley & Sons, Ltd.
- Schlenker, J. L., Gibbs, G. V. & Boisen, M. B. (1975). *Am. Mineral.* **60**, 828–833.
- Sears, V. F. (1992). *Neutron News*, **3**, 26–37.
- Seymour, K. C., Hughes, R. W. & Kriven, W. M. (2015). *J. Am. Ceram. Soc.* **98**, 4096–4101.
- Seymour, K. C., Ribero, D., McCormack, S. J. & Kriven, W. M. (2016). *J. Am. Ceram. Soc.* **99**, 3739–3744.
- Shcherbakova, L. G., Mamsurova, L. G. & Sukhanova, G. E. (1979). *Russ. Chem. Rev.* **48**, 228–242.
- Shlyakhtina, A. V., Fedtke, P., Busch, A., Kolbanev, I. V., Barfels, T., Wienecke, M., Sokolov, A. E., Ulianov, V. A., Trounov, V. A. & Shcherbakova, L. G. (2008). *Solid State Ionics*, **179**, 1004–1008.
- Shlyakhtina, A. V., Karyagina, O. K. & Shcherbakova, L. G. (2004). *Inorg. Mater.* **40**, 59–65.
- Shlyakhtina, A. V. & Shcherbakova, L. G. (2012). *Russ. J. Electrochem.* **48**, 1–25.
- Sinha, A. & Sharma, B. P. (2005). *J. Am. Ceram. Soc.* **88**, 1064–1066.
- Sosin, S. S., Prozorova, L. A., Smirnov, A. I., Golov, A. I., Berkutov, I. B., Petrenko, O. A., Balakrishnan, G. & Zhitomirsky, M. E. (2005). *Phys. Rev. B Condens. Matter Mater. Phys.* **71**, 1–5.
- Subramanian, M. A., Aravamudan, G. & Subba Rao, G. V. (1983). *Prog. Solid State Chem.* **15**, 55–143.
- Tanaka, M., Sekii, H. & Ohi, K. (1985). *Jpn. J. Appl. Phys.* **24**, 814–816.
- Taylor, R. (1998). *Thermal Expansion of Solids, CINDAS Data Series on Materials Properties*. Materials Park, OH: ASM International.
- Teterin, G. A., Zinchenko, V. F., Zagorodnyuk, A. V. & Minaev, I. M. (1988). *Ukr. Chem. J.* **54**, 252–255.
- Toby, B. H. (2006). *Powder Diffr.* **21**, 67–70.
- Toby, B. H. & Von Dreele, R. B. (2013). *J. Appl. Cryst.* **46**, 544–549.
- Touloukian, Y. S. (1975). *Thermal Expansion: Metallic Elements and Alloys*. New York, NY: Plenum Publishing Corporation.
- Turner, R. C., Fuierer, P. A., Newnham, R. E. & Shrout, T. R. (1994). *Appl. Acoust.* **41**, 299–324.
- Uno, W., Fujii, K., Niwa, E., Torii, S., Miao, P., Kamiyama, T. & Yashima, M. (2018). *J. Ceram. Soc. Japan*, **126**, 341–345.
- van Dijk, M. P., ter Maat, J. H. H., Roelofs, G., Bosch, H., van de Velde, G. M. H., Gellings, P. J. & Burggraaf, A. J. (1984). *Mat. Res. Bull.* **19**, 1149–1156.
- Weber, T., Harz, M., Wehner, B., Zahn, G. & Paufler, P. (1998). *Z. Kristallogr.* **213**, 210–216.
- Wuensch, B. J., Eberman, K. W., Heremans, C., Ku, E. M., Onnerud, P., Yeo, E. M. E., Haile, S. M., Stalick, J. K. & Jorgensen, J. D. (2000). *Solid State Ionics*, **129**, 111–133.
- Yamamura, H., Nishino, H., Kakinuma, K. & Nomura, K. (2003). *Solid State Ionics*, **158**, 359–365.
- Yan, H., Ning, H., Kan, Y., Wang, P. & Reece, M. J. (2009). *J. Am. Ceram. Soc.* **92**, 2270–2275.
- Zhang, F. X., Lian, J., Becker, U., Ewing, R. C., Wang, L. M., Hu, J. & Saxena, S. K. (2007). *J. Solid State Chem.* **180**, 571–576.
- Zhou, Z., Palatinus, L. & Sun, J. (2016). *Inorg. Chem. Front.* **3**, 1351–1362.